Chiral Light Emission from a Sphere Revealed by Nanoscale Relative-Phase Mapping

– SUPPORTING INFORMATION –

Taeko Matsukata,[1,2] F. Javier García de Abajo,[3,4] and Takumi Sannomiya[1,5]

[1] *Department of Materials Science and Technology, Tokyo Institute of Technology, 4259 Nagatsuta Midoriku, Yokohama 226-8503, Japan*
[2] *RIKEN, 2-1 Hirosawa, Wako, Saitama 351-0198, Japan*
[3] *ICFO-Institut de Ciencies Fotoniques, The Barcelona Institute of Science and Technology, 08860 Castelldefels (Barcelona), Spain*
[4] *ICREA-Institució Catalana de Recerca i Estudis Avançats, Passeig Lluís Companys 23, 08010 Barcelona, Spain*
[5] *PRESTO, 4259 Nagatsuta Midoriku, Yokohama 226-8503, Japan*

(Dated: September 12, 2020)

CONTENTS

1. DATA ANALYSIS OF ANGLE- AND ENERGY-RESOLVED PATTERNS

On the 2D CCD of the spectrometer in the 4D STEM-CL setup, information on energy is encoded in the horizontal direction while information on the angle θ is mapped onto the vertical axis. In practice, the chromatic aberration induced by the measurement optics in the optical path to the CCD camera makes the magnification of the image dependent on energy. To properly obtain the spectrum at a certain angle θ, we need to extract the signal at a different vertical position for each energy on the CCD plane, with the chromatic aberration taken into account. We correct this vertical shift by performing a calibration by fitting the energy dispersion curves with a model function of θ. The angle θ is assumed to be mapped to the position y on the CCD camera through the following function, based on the lens maker's equation and using the mask position p, corresponding to the angle θ, on the mask plane:

$$y = [A\, n(\lambda) + B]\, \tan^{-1}\left[(p - p_0)/C\right] + D, \tag{S1}$$

where $n(\lambda)$ is the wavelength-dependent refractive index of the used lens (fused silica) and p_0 is the offset from the true optical axis. The fitting parameters A, B, C, and D are obtained by adjusting the experimental energy dispersion curves using the least square method. First, for obtaining a calibration dataset (energy dispersion curves), the pinhole mask for angle selection is set at the mask position, from where it is then scanned from the bottom to the top of the mirror to measure CCD images at each angle. The CCD image obtained at each pinhole mask position shows the trace of the corresponding angle θ at each energy, thus determining the projection position on the CCD plane at a certain angle and a certain energy. Figure S1 shows an example of the obtained fitting curves. The displayed image is the sum of data acquired at all angles, while the fitted curves are superimposed as horizontal yellow lines in Figure

S1. The effectiveness of the fitting curve is confirmed by matching the position of the upper and lower holes of the mirror for the electron beam path to $\theta = 0$ and 180°, respectively, and the sample shadow to $\theta = 90°$ (horizontal lines in Figure S1). The parameter p_0 is adjusted manually to best match all the fitting curves. This fitting function is used to extract accurate data at a specific angle and energy. In order to remove noise from the CCD image, a 2D wavelet-denoising process is followed.

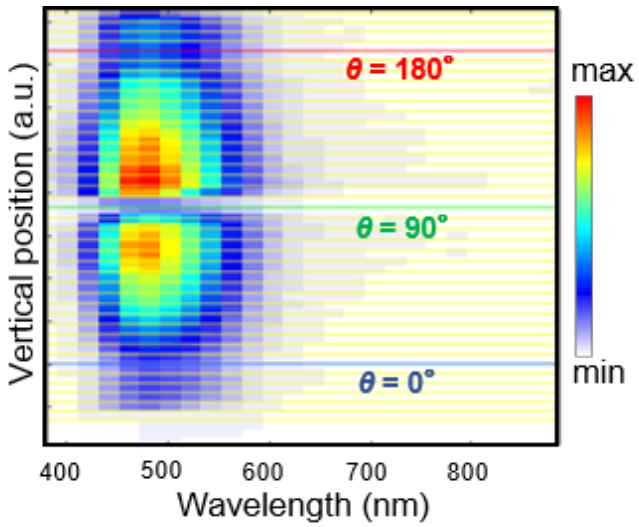

Figure S1. Signal extraction after correcting for chromatic aberration based on Eq. (S1). The horizontal yellow lines are the fits to the data. The blue, green, and red horizontal lines correspond to fitted spectral curves at angles $\theta = 0°$, 90°, and 180°, respectively.

2. PHASE SHIFT CAUSED BY THE ALUMINUM PARABOLIC MIRROR

We correct for the phase shift due to reflection on the aluminum parabolic mirror to appropriately obtain the relative phase δ. The polarization state is affected by this reflection due to the angle-dependent phase difference between s- and p-polarized light. Since the experimentally measured phase difference δ is directly affected by this reflection phase shift, we correct δ at each angle and energy using the calculated reflection phase shift as shown in Figure S2. We find the reflection phase to be close to π for all energies and angles, with slight deviations from this value at directions near perpendicular emission ($\theta = 0°$ and 180°). Observing the emitted photons from the detector, s-polarized light undergoes a phase shift π with respect to p-polarized light at normal reflection ($\theta = 90°$), which corresponds to an inversion of the handedness of CPL upon reflection.

3. 4D DATASET OF CL MAPS

The proposed 4D STEM-CL allows us to collect CL maps at all energies and angles θ simultaneously. Actually, through a single raster scan for mapping, we can obtain a dataset map that consists of 255 angles × 1024 photon energies at maximum resolution. In practice, we reduce the data size, reduce the noise, and speed up the readout by acquiring 51×256 (=13,056) photon maps (*i.e.*, binning 5 pixels in the vertical direction (angle) and 4 pixels in the horizontal direction (energy)). Parts of such mapping datasets are shown in Figures S3, S4, and S5.

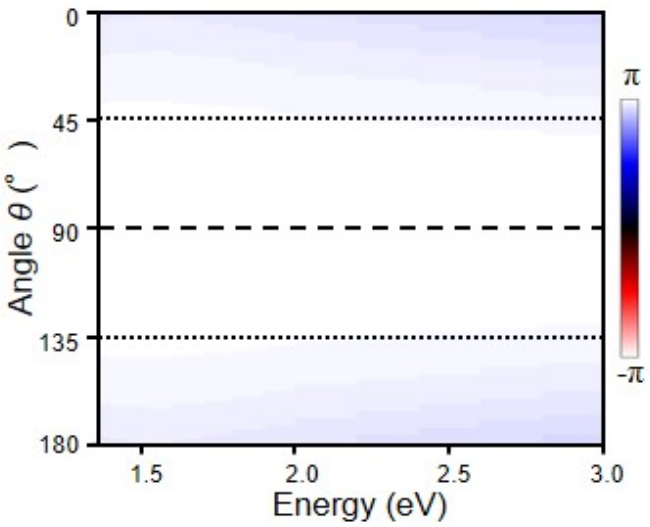

Figure S2. Dependence of the phase shift produced by the aluminum mirror on photon energy and emission angle θ.

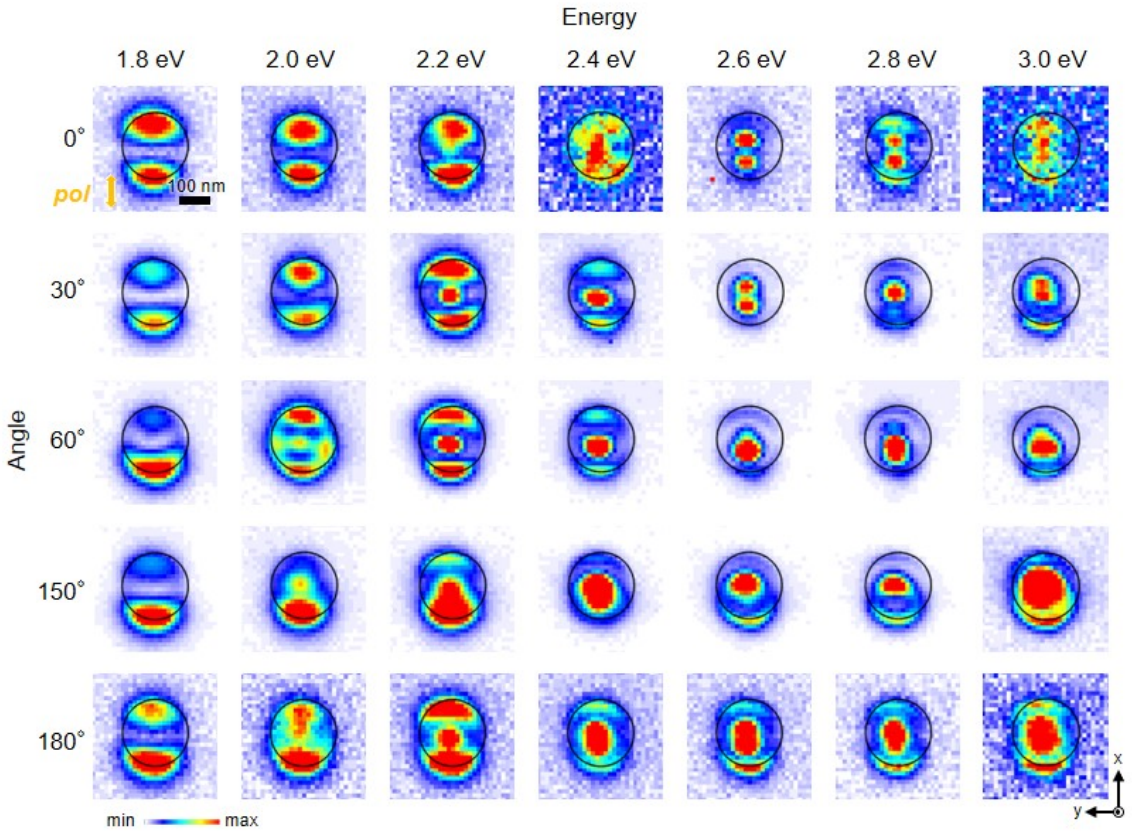

Figure S3. Simultaneously obtained photon maps with 0°-polarization.

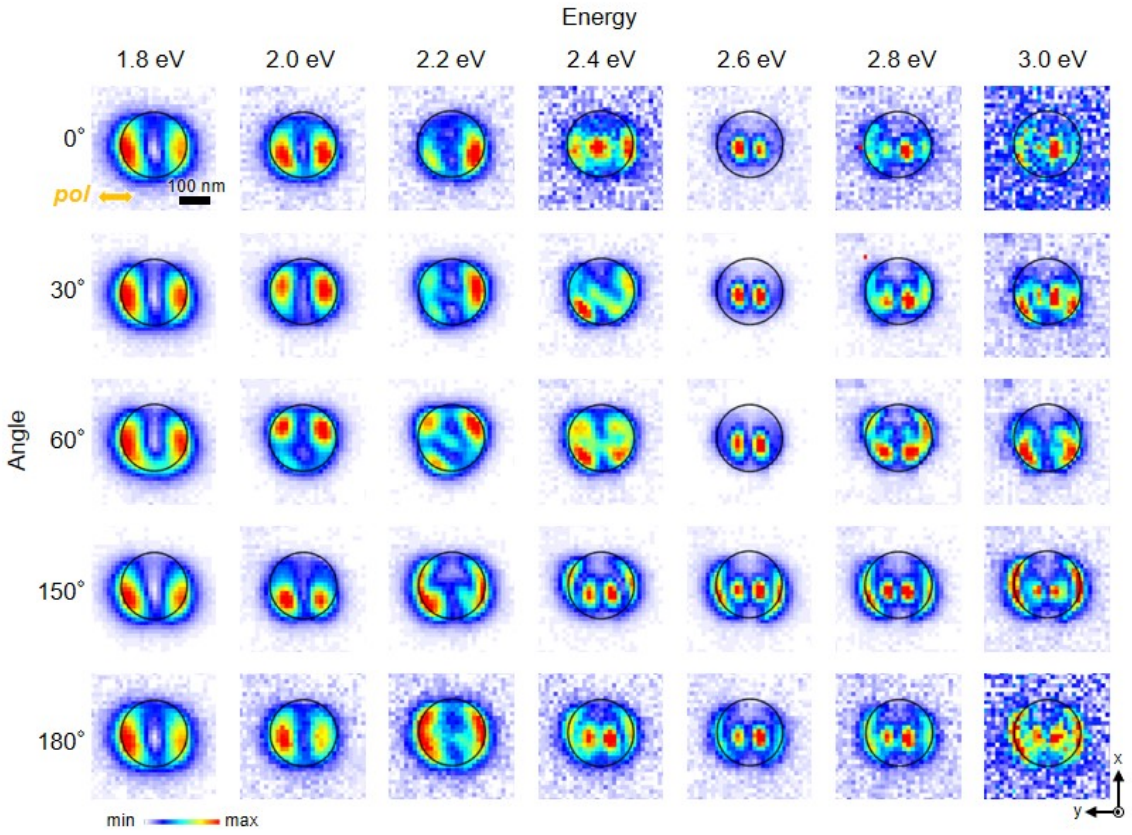

Figure S4. Simultaneously obtained photon maps with 90°-polarization.

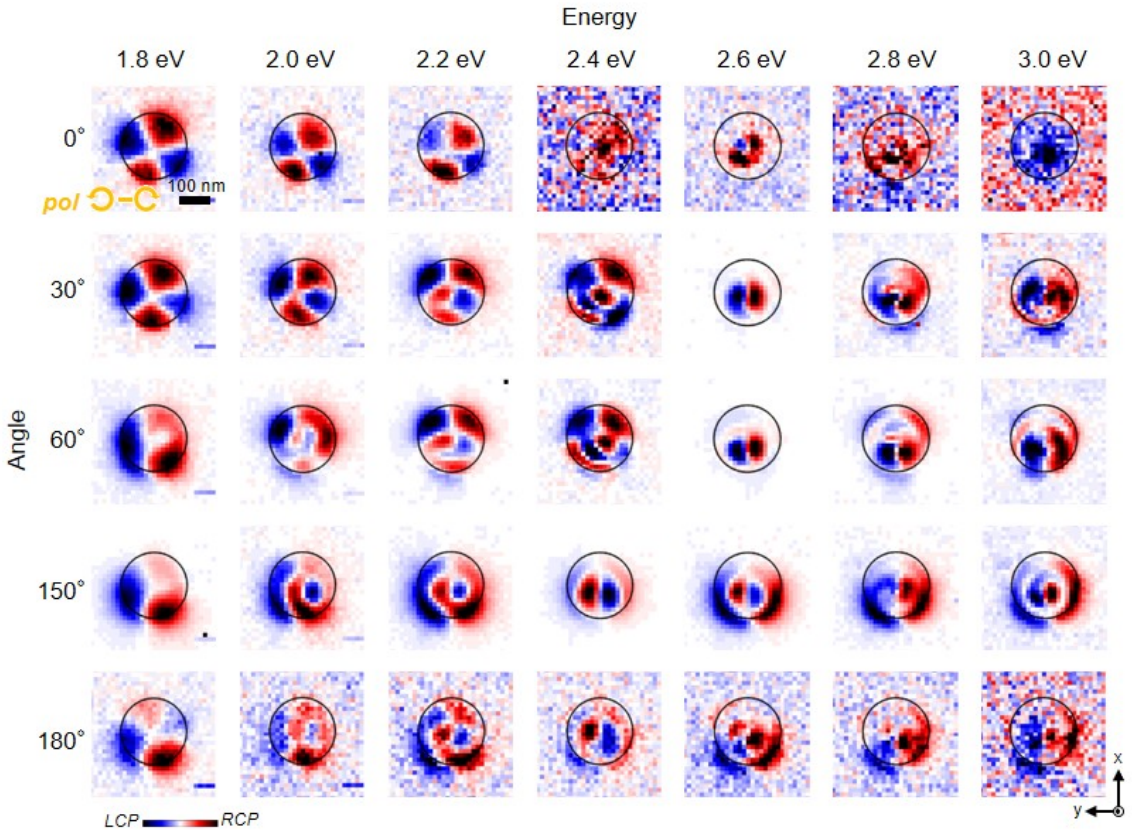

Figure S5. Simultaneously obtained photon maps of S_3.

4. ANALYTICAL MULTIPOLE DECOMPOSITION (AMD)

We are interested in calculating the far field produced by the passage of an electron through a self-standing sphere, as shown in Figure S6. We assume that the sphere of radius a centered at the origin can be described by a local, frequency-dependent permittivity $\epsilon(\omega)$, while the electron with the elementary charge $-e$ is treated as a classical point charge following a straight-line trajectory with constant velocity vector $\mathbf{v} = v\hat{\mathbf{z}}$. The time-dependent electron position is then $\mathbf{r}_t = (\mathbf{R}_0, vt)$, where $\mathbf{R}_0 = (x_0, y_0)$ is an impact parameter vector in the plane perpendicular to the trajectory and the electron reaches its minimum distance to the sphere center at $t = 0$. In our analysis, we first consider an electron moving inside a homogeneous material and decompose the external electric field that it produces as[1]

$$\mathbf{E}^{\rm ext}(\mathbf{r},t) = \int \frac{d\omega}{2\pi}\, \mathbf{E}^{\rm ext}(\mathbf{r},\omega)\, \mathrm{e}^{-\mathrm{i}\omega t},$$

where

$$\begin{aligned}\mathbf{E}^{\rm ext}(\mathbf{r},\omega) &= e\left(\frac{1}{\epsilon}\nabla - \frac{\mathrm{i}k\mathbf{v}}{c}\right)\int dt\, \mathrm{e}^{\mathrm{i}\omega t}\frac{\mathrm{e}^{\mathrm{i}k'|\mathbf{r}-\mathbf{r}_t|}}{|\mathbf{r}-\mathbf{r}_t|} \\ &= 4\pi e k'\left(\frac{1}{\epsilon}\nabla - \frac{\mathrm{i}k\mathbf{v}}{c}\right)\int dt\, \mathrm{e}^{\mathrm{i}\omega t}\sum_L j_l(k'r_<)h_l^{(+)}(k'r_>)Y_L(\Omega_{\hat{\mathbf{r}}})Y_L^*(\Omega_{\hat{\mathbf{r}}_t}),\end{aligned} \tag{S2}$$

$k = \omega/c$, $k' = k\sqrt{\epsilon}$, $r_< = \min\{r, r_t\}$, $r_> = \max\{r, r_t\}$, $L = (l, m)$ runs over angular momentum components with $l = 0, 1, \ldots$ and $|m| \leq l$, Y_L are spherical harmonics, and j_l and $h_l^{(+)}$ are spherical Bessel and Hankel functions, respectively.

We now divide the problem into two contributions corresponding to inner and outer parts of the electron trajectory, as illustrated in Figure S6. In particular, the outer trajectory (electron in the vacuum region II) produces an external field outside and near the sphere surface given by

$$\mathbf{E}^{\rm ext,II}(\mathbf{r},\omega) = e\left(\nabla - \frac{\mathrm{i}k\mathbf{v}}{c}\right)\sum_L j_l(kr)Y_L(\Omega_{\hat{\mathbf{r}}})\phi_L^{\rm II} \tag{S3}$$

with

$$\begin{aligned}\phi_L^{\rm II} &= 4\pi k\left[\int_{-\infty}^{\infty} dt\, \mathrm{e}^{\mathrm{i}\omega t}\sum_L h_l^{(+)}(kr_t)Y_L^*(\Omega_{\hat{\mathbf{r}}_t}) - \int_{-z_0/v}^{z_0/v} dt\, \mathrm{e}^{\mathrm{i}\omega t}\sum_L h_l^{(+)}(kr_t)Y_L^*(\Omega_{\hat{\mathbf{r}}_t})\right] \\ &= 4\pi k\left[\frac{A_L^+}{\omega}K_m\left(\frac{\omega R_0}{v\gamma}\right)\mathrm{e}^{-\mathrm{i}m\varphi_0} - \int_{-z_0/v}^{z_0/v} dt\, \mathrm{e}^{\mathrm{i}\omega t}\sum_L h_l^{(+)}(kr_t)Y_L^*(\Omega_{\hat{\mathbf{r}}_t})\right],\end{aligned}$$

where $z_0 = \sqrt{a^2 - R_0^2}$ is the point at which the electron crosses the sphere surface and the second line incorporates the analytical solution of the first integral[1, 2] in terms of the coefficients A_L^+ defined as

$$A_L^+ = \mathrm{i}^{l+m}(2m-1)!!\sqrt{\frac{(2l+1)(l-m)!}{\pi(l+m)!}}\frac{(c/v)^{m+1}}{\gamma^m}\, C_{l-m}^{m+1/2}\Big[\frac{c}{v}\Big]$$

for $m \geq 0$ and satisfying $A_{l,-m}^+ = (-1)^m A_{l,m}^+$. Here, $C_\nu^\mu[x]$ are Gegenbauer polynomials,[3, 4] $\gamma = 1/\sqrt{1 - v^2/c^2}$, and φ_0 is the azimuthal angle of $\mathbf{R}_0$. Equation (S3) allows us to write a multipolar decomposition of the field outside and near the sphere surface as[1, 5]

$$\mathbf{E}^{\rm ext,II}(\mathbf{r},\omega) = \mathbf{L}\psi^{\rm M,ext,II} - \frac{\mathrm{i}}{k}\nabla\times\mathbf{L}\psi^{\rm E,ext,II}, \tag{S4}$$

in terms of the angular momentum operator $\mathbf{L} = -\mathrm{i}\mathbf{r}\times\nabla$ and the scalar functions

$$\psi^{\nu,\rm ext,II} = \sum_L \mathrm{i}^l j_l(kr)Y_L(\Omega_{\mathbf{r}})\psi_L^{\nu,\rm ext,II}$$

with expansion coefficients $\psi_L^{\nu,\rm ext,II}$ determined from the relations $\psi^{\rm M} = (1/L^2)\mathbf{L}\cdot\mathbf{E}$ and $\psi^{\rm E} = (\mathrm{i}/kL^2)(\mathbf{L}\times\nabla)\cdot\mathbf{E}$. Inserting Eq. (S3) into these expressions, substituting the squared operator L^2 by $l(l+1)$ in each L term, and using

the recursion properties of the spherical Bessel and Hankel functions in a way similar to previous work,[1] we find after some algebra

$$\psi_L^{M,\mathrm{ext,II}} = -\mathrm{e}^{-\mathrm{i}m\varphi_0}\frac{4\pi \mathrm{i}^{1-l} mek}{l(l+1)c}\left[\frac{v}{c}A_L^+ K_m\left(\frac{\omega R_0}{v\gamma}\right) - k\int_{-z_0}^{z_0} dz\,\mathrm{e}^{\mathrm{i}\omega z/v} h_l^{(+)}(kr)Y_L(\theta,0)\right], \tag{S5a}$$

$$\begin{aligned}\psi_L^{E,\mathrm{ext,II}} = -\mathrm{e}^{-\mathrm{i}m\varphi_0}\frac{2\pi \mathrm{i}^{1-l} ek}{l(l+1)c}\Bigg\{&\frac{1}{\gamma}B_L K_m\left(\frac{\omega R_0}{v\gamma}\right) \\ &- \frac{1}{R_0}\int_{-z_0}^{z_0} dz\,\mathrm{e}^{\mathrm{i}\omega z/v}\Big[C_L^-(R_0\partial_{R_0}+1-m)h_l^{(+)}(kr)Y_{l,m-1}(\theta,0) \\ &\qquad - C_L^+(R_0\partial_{R_0}+1+m)h_l^{(+)}(kr)Y_{l,m+1}(\theta,0)\Big]\Bigg\},\end{aligned} \tag{S5b}$$

where

$$C_L^{\pm} = \sqrt{(l\pm m+1)(l\mp m)}, \tag{S6}$$

$$B_L = C_L^+ A_{l,m+1}^+ - C_L^- A_{l,m-1}^+, \tag{S7}$$

$r = \sqrt{R_0^2+z^2}$, and $\theta = \cos^{-1}(z/r)$.

The induced field produced upon scattering by the sphere admits the same decomposition as in Eq. (S4) with $\psi^{\nu,\mathrm{ext,II}}$ replaced by[1]

$$\psi^{\nu,\mathrm{ind,II}} = \sum_L \mathrm{i}^l h_l^{(+)}(kr)Y_L(\Omega_{\mathbf{r}})\psi_L^{\nu,\mathrm{ind,II}}, \tag{S8}$$

where

$$\psi_L^{\nu,\mathrm{ind,II}} = t_l^{\nu}\psi_L^{\nu,\mathrm{ext,II}}$$

and

$$t_l^{\mathrm{M}} = \frac{-\rho_1 j_l(\rho_0)j_l'(\rho_1) + \rho_0 j_l(\rho_1)j_l'(\rho_0)}{\rho_1 h_l^{(+)}(\rho_0)j_l'(\rho_1) - \rho_0 j_l(\rho_1)[h_l^{(+)}(\rho_0)]'}, \tag{S9a}$$

$$t_l^{\mathrm{E}} = \frac{-j_l(\rho_0)[j_l(\rho_1)+\rho_1 j_l'(\rho_1)] + \epsilon j_l(\rho_1)[j_l(\rho_0)+\rho_0 j_l'(\rho_0)]}{h_l^{(+)}(\rho_0)[j_l(\rho_1)+\rho_1 j_l'(\rho_1)] - \epsilon j_l(\rho_1)\{h_l^{(+)}(\rho_0)+\rho_0[h_l^{(+)}(\rho_0)]'\}} \tag{S9b}$$

are Mie scattering coefficients in which $\rho_0 = ka$, $\rho_1 = ka\sqrt{\epsilon}$, and the prime denotes differentiation with respect to the argument (ρ_0 or ρ_1 in each case). Here, square roots are taken to yield positive real parts.

The induced field receives an additional contribution from the inner part of the trajectory (see Figure S6). From Eq. (S2), the corresponding external field inside and near the sphere surface admits the expression

$$\mathbf{E}^{\mathrm{ext,I}}(\mathbf{r},\omega) = e\left(\frac{1}{\epsilon}\nabla - \frac{\mathrm{i}k\mathbf{v}}{c}\right)\sum_L h_l^{(+)}(k'r)Y_L(\Omega_{\hat{\mathbf{r}}})\phi_L^{\mathrm{I}}$$

with

$$\phi_L^{\mathrm{I}} = 4\pi k'\int_{-z_0/v}^{z_0/v} dt\,\mathrm{e}^{\mathrm{i}\omega t}\sum_L j_l(k'r_t)Y_L^*(\Omega_{\hat{\mathbf{r}}_t}).$$

Now, performing a similar multipolar expansion for this inner part of the trajectory as done above for the outer part, we find $\mathbf{E}^{\mathrm{ext,I}}(\mathbf{r},\omega) = \mathbf{L}\psi^{\mathrm{M,ext,I}} - (\mathrm{i}/k)\nabla\times\mathbf{L}\psi^{\mathrm{E,ext,I}}$ with scalar functions

$$\psi^{\nu,\mathrm{ext,I}} = \sum_L \mathrm{i}^l h_l^{(+)}(k'r)Y_L(\Omega_{\mathbf{r}})\psi_L^{\nu,\mathrm{ext,I}}$$

and expansion coefficients

$$\psi_L^{M,\mathrm{ext,I}} = -\mathrm{e}^{-\mathrm{i}m\varphi_0}\frac{4\pi\mathrm{i}^{1-l}mek}{l(l+1)c}k'\int_{-z_0}^{z_0}dz\,\mathrm{e}^{\mathrm{i}\omega z/v}j_l(k'r)Y_L(\theta,0), \tag{S10a}$$

$$\psi_L^{E,\mathrm{ext,I}} = -\mathrm{e}^{-\mathrm{i}m\varphi_0}\frac{2\pi\mathrm{i}^{1-l}ek}{l(l+1)c}\,\frac{1}{\sqrt{\epsilon}R_0}\int_{-z_0}^{z_0}dz\,\mathrm{e}^{\mathrm{i}\omega z/v}\Big[C_L^-(R_0\partial_{R_0}+1-m)j_l(k'r)Y_{l,m-1}(\theta,0) - C_L^+(R_0\partial_{R_0}+1+m)j_l(k'r)Y_{l,m+1}(\theta,0)\Big]. \tag{S10b}$$

This induced field is transmitted from inside to outside the sphere in the form of outgoing waves similar to those of Eq. (S8) with coefficients

$$\psi_L^{\nu,\mathrm{ind,I}} = B_l^\nu\psi_L^{\nu,\mathrm{ext,I}},$$

where

$$B_l^{\mathrm{M}} = -\rho_1\,\frac{h_l^{(+)}(\rho_1)j_l'(\rho_1) - j_l(\rho_1)[h_l^{(+)}(\rho_1)]'}{\rho_0 j_l(\rho_1)[h_l^{(+)}(\rho_0)]' - \rho_1 h_l^{(+)}(\rho_0)j_l'(\rho_1)}, \tag{S11a}$$

$$B_l^{\mathrm{E}} = -\epsilon\rho_1\,\frac{h_l^{(+)}(\rho_1)j_l'(\rho_1) - j_l(\rho_1)[h_l^{(+)}(\rho_1)]'}{\epsilon j_l(\rho_1)\{h_l^{(+)}(\rho_0)+\rho_0[h_l^{(+)}(\rho_0)]'\} - h_l^{(+)}(\rho_0)[j_l(\rho_1)+\rho_1 j_l'(\rho_1)]} \tag{S11b}$$

are Mie transmission coefficients.

The above contributions to the induced field produced outside the sphere refer to the direct field of the electron in the outer and inner parts of the trajectory after scattering or transmission *via* the corresponding Mie coefficients. There is however an additional contribution indicated with a second red arrow in the central sphere of Figure S6 corresponding to the direct field produced by the interrupted outer trajectory of the electron, which, unlike the infinite electron trajectory, gives rise to a finite contribution to the far-field cathodoluminescence (CL) emission. This contribution is the sum of the field produced by an infinite trajectory (which does not produce a propagating far field, but only an evanescent field accompanying the electron) minus the field produced by a finite electron trajectory of the same extension as the inner part considered above, but now evaluated in a vacuum. The resulting contribution to the far field is then similar to that of Eqs. (S10) (*i.e.*, evaluated at positions of radial vector larger than those of the source), but with the permittivity set to the vacuum value $\epsilon = 1$. This leads to an additional contribution

$$\psi_L^{M,\mathrm{ind,II,direct}} = -\mathrm{e}^{-\mathrm{i}m\varphi_0}\frac{4\pi\mathrm{i}^{1-l}mek}{l(l+1)c}(-k)\int_{-z_0}^{z_0}dz\,\mathrm{e}^{\mathrm{i}\omega z/v}j_l(kr)Y_L(\theta,0), \tag{S12a}$$

$$\psi_L^{E,\mathrm{ind,II,direct}} = -\mathrm{e}^{-\mathrm{i}m\varphi_0}\frac{2\pi\mathrm{i}^{1-l}ek}{l(l+1)c}\,\left(\frac{-1}{R_0}\right)\int_{-z_0}^{z_0}dz\,\mathrm{e}^{\mathrm{i}\omega z/v}\Big[C_L^-(R_0\partial_{R_0}+1-m)j_l(kr)Y_{l,m-1}(\theta,0) - C_L^+(R_0\partial_{R_0}+1+m)j_l(kr)Y_{l,m+1}(\theta,0)\Big] \tag{S12b}$$

to the induced far field.

Finally, we can calculate the frequency- and angle-dependent far-field CL scattering amplitude as[6]

$$\mathbf{f}_{\mathrm{CL}}(\Omega,\omega) = \frac{1}{k}\sum_L\left[\vec{\zeta}_L(\Omega)\psi_L^{\mathrm{M,ind}} + \hat{\mathbf{r}}\times\vec{\zeta}_L(\Omega)\psi_L^{\mathrm{E,ind}}\right], \tag{S13}$$

where we define the vector spherical harmonics

$$\vec{\zeta}_L(\Omega) = \mathbf{L}Y_L(\Omega) = \frac{1}{2}\left[C_L^-Y_{l,m-1}(\Omega) + C_L^+Y_{l,m+1}(\Omega)\right]\,\hat{\mathbf{x}} + \frac{\mathrm{i}}{2}\left[C_L^-Y_{l,m-1}(\Omega) - C_L^+Y_{l,m+1}(\Omega)\right]\,\hat{\mathbf{y}} + mY_L(\Omega)\,\hat{\mathbf{z}}.$$

The multipolar coefficients of the induced field in Eq. (S13) are given by the sum of all of the above contributions as

$$\psi_L^{\nu,\mathrm{ind}} = B_l^\nu\psi_L^{\nu,\mathrm{ext,I}} + t_l^\nu\psi_L^{\nu,\mathrm{ext,II}} + \psi_L^{\nu,\mathrm{ind,II,direct}},$$

where the different elements are defined in Eqs. (S5), (S6), (S7), (S9), (S10), (S11), and (S12). Equation (S13) directly allows us to calculate the contribution to the far field amplitude originating in different multipoles. It also allows us

to obtain the polarization of the emitted light. The CL photon emission probability is then obtained from the far-field Poynting vector divided by the photon energy $\hbar\omega$,[1] which leads to

$$\Gamma_{\rm CL}(\Omega,\omega) = \frac{1}{4\pi^2\hbar k}|\mathbf{f}_{\rm CL}(\Omega,\omega)|^2.$$

This quantity is normalized in such a way that the integral over angle and frequency $\int d\Omega \int_0^\infty d\omega \Gamma_{\rm CL}(\Omega,\omega)$ yields the total photon emission probability. We can further use the orthogonality relations of the vector spherical harmonics $\int d\Omega\, \vec{\zeta}_L(\Omega)\cdot\vec{\zeta}_{L'}(\Omega) = \int d\Omega\, [\hat{\mathbf{r}}\times\vec{\zeta}_L(\Omega)]\cdot[\hat{\mathbf{r}}\times\vec{\zeta}_{L'}(\Omega)] = l(l+1)\delta_{L,L'}$ and $\int d\Omega\, \vec{\zeta}_L(\Omega)\cdot[\hat{\mathbf{r}}\times\vec{\zeta}_{L'}(\Omega)] = 0$ to calculate the angle-integrated CL photon emission probability

$$\Gamma_{\rm CL}(\omega) = \int d\Omega \Gamma_{\rm CL}(\Omega,\omega) = \frac{1}{4\pi^2\hbar k^3}\sum_{L,\nu} l(l+1)\left|\psi_L^{\nu,\rm ind}\right|^2,$$

where the sum runs over electric (ν =E) and magnetic (ν =M) multipoles $L=(l,m)$.

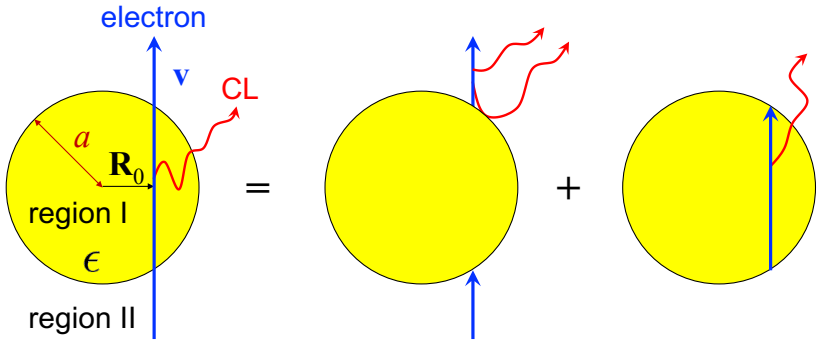

Figure S6. Elements involved in the description of CL emission by an electron traversing a homogeneous sphere. The emission is decomposed into the contributions coming from the inner and outer parts of the electron trajectory.

5. COMPARISON OF THE CL SPECTRA BY AMD CALCULATION AND THE OPTICAL SCATTERING CROSS SECTION BY MIE CALCULATION

In this section, we show the CL intensity spectra obtained by using the AMD approach for particles of the same size as those used in experiment (250 nm and 170 nm, see STEM images in Figures 3a and 8a) and compare them to the scattering cross-section spectra obtained from Mie theory under plane-wave light irradiation. Figures S7a and b show CL spectra integrated in emission directions (θ = 0-180°, ϕ = 0-360°) and averaged over electron beam positions scanning the entire particle, as calculated from the AMD method. The results are in good agreement with the measured CL intensity spectra shown in the main text (Figures 2c and 8c). We attribute the slight blue shifts observed in the calculated spectrum compared to experiment to an overestimate of the particle size in the latter, and a possible effect of surface oxidation. In conventional Mie scattering calculations for dielectric spheres, there are some notable features found in the scattering spectra, such as an *anapole* that involves no radiation and results in dips in the scattering cross section. Here, we focus on this anapole feature and compare AMD calculations to Mie scattering calculations. Although the CL spectra obtained by the AMD method exhibit similar shapes to the scattering cross-section spectra obtained from Mie theory (Figures S7c and d), there are some remarkable differences, especially for ED modes. The ED modes with different radial orders cancel each other at certain energies, resulting in zero radiation emission; this condition coincides with non-radiative dips in the Mie calculation around 2.0 eV in Figure S7c and 2.5 eV in Figure S7d. In contrast, the AMD calculations (Figures S7a and b) show no such feature. This difference must originate in the excitation source: the Mie calculation incorporates a plane wave excitation that involves only $m = \pm 1$ modes (*e.g.*, *i*ED, but not *p*ED with $m = 0$) due to the symmetry of the plane wave; in the AMD calculation a point-source-like electron beam moving along the z direction can excite different modes, including *p*ED, depending on the electron beam position.

To understand this phenomenon in more detail, we compare the profiles of *p*ED and *i*ED modes as we change the excitation beam position from the center to the edge of the sphere. Figure S7e summarizes the spectral changes of ED (*i*ED + *p*ED) modes at different excitation beam positions (radius distance r = 4-124 nm). An anapole like feature (dip in the spectrum) is found around 2 eV when excited at the edge (blue curve in Figure S7e), which starts

disappearing as the beam is moved inside the sphere, and then reappears at 1.7 eV as the beam continues to approach the sphere center. This position-dependent spectra of the ED^1 mode explain why there is no clear anapole dip in the spatially integrated spectra in Figures S7a and b.

To clarify the contributions of pED^1 and iED^1 modes, spectra of each component are separately plotted in Figures S7f and g, respectively. In the iED spectra (Figure S7g), the anapole feature appears around 2.0 eV and is present only when exciting near the edge, but it disappears when the beam approaches the sphere center. The spectra with the beam near the sphere edge are similar to the optical scattering cross section calculated from Mie theory, where the ED^2 mode is excited through the field at the edges and its far-field is canceled out by the ED^1 mode. Indeed, this anapole energy of 2.0 eV in the CL calculation matches that of Mie scattering theory in Figure S7c. However, when excited near the center, no anapole-like feature appear in the spectra. We attribute this effect to the selective excitation of the internal dipole of iED^2, which is possible only by the electron beam, and also, the phase of the ED^2 mode coincides with the ED^1 phase, resulting in no far-field cancellation. This phase flip of iED^2 depending on the beam position can be experimentally seen in the mapping shown in Figure 5 in the main text. Interestingly, the *anapole* dips of pED modes keep appearing for all beam positions at different photon energies in the 1.7-2.0 eV range, as shown in Figure S7f. This implies that the phase of the field at the outermost layer is almost constant regardless of the beam position. The shift in dip energy can be attributed to a phase shift of pED around 1.7-2.0 eV, as shown in Figure S9. To grasp the radiation of each mode, we also show the radiation pattern of each mode resolved by polarization in Figure S8.

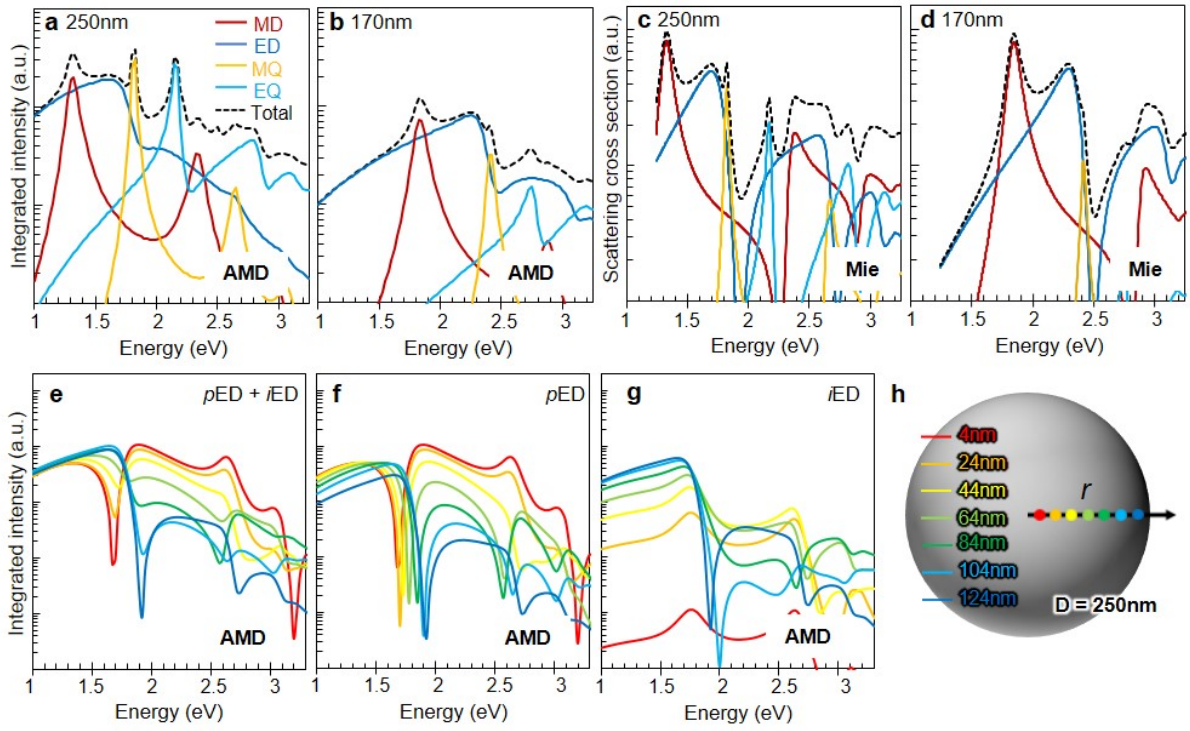

Figure S7. Comparison between AMD and Mie calculations for CL and light scattering, respectively. (a,b) CL spectra integrated over all emission angles and beam positions on the sphere, calculated by using the AMD approach for (a) 250 nm and (b) 170 nm Si spheres. (c,d) Mie scattering cross-section spectra of (c) 250 nm and (d) 170 nm Si spheres. (e-g) AMD-calculated partial CL spectra contributed by (e) ED (iED + pED), (f) pED, and (g) iED with the excitation beam position at radius r varying from 4nm (red curve) to 124 nm (dark blue curve). The diameter of the Si nanosphere is 250 nm. (h) Illustration of the color-coordinated beam positions considered in the spectra plotted in (e-g).

6. SIMULATED PHASE LINE PROFILES

This section provides additional information supporting the discussion of the spectral line profiles of the emission phase calculated by using the AMD approach in the main text (Figure 4). The spectral line profiles of the phase of p- and s-polarization emission components, together with the phase difference δ, are calculated including multipoles up

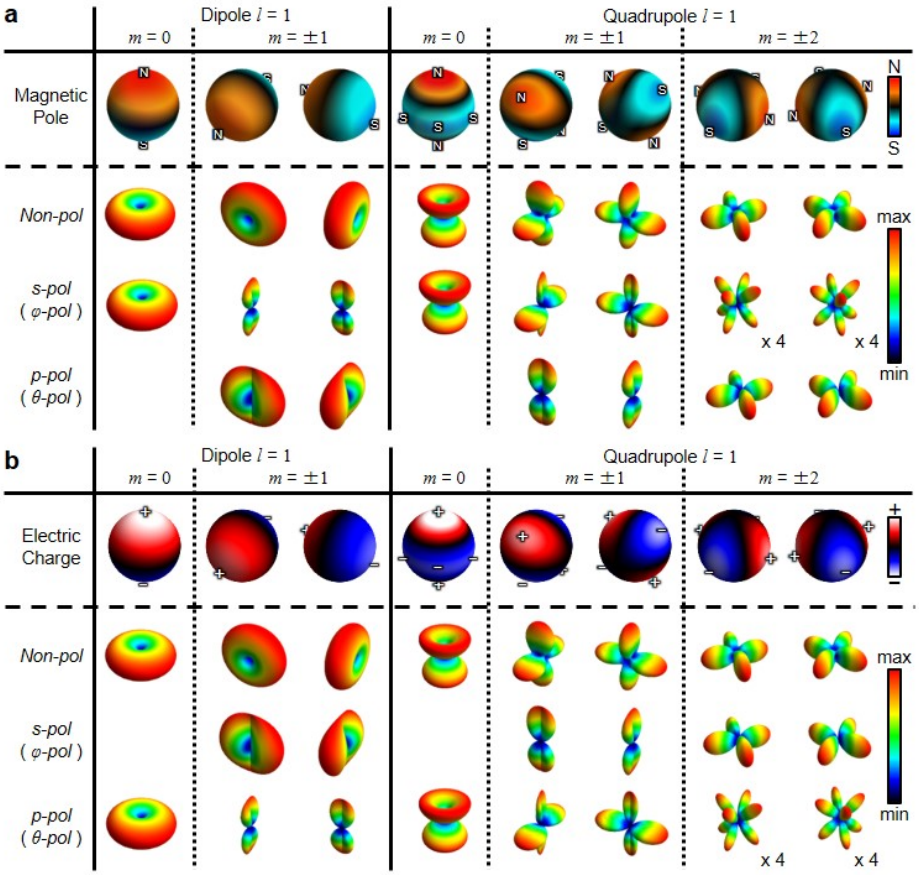

Figure S8. Angular distribution of (a) magnetic and (b) electric charges, along with their radiation patterns for different detector-selected polarizations.

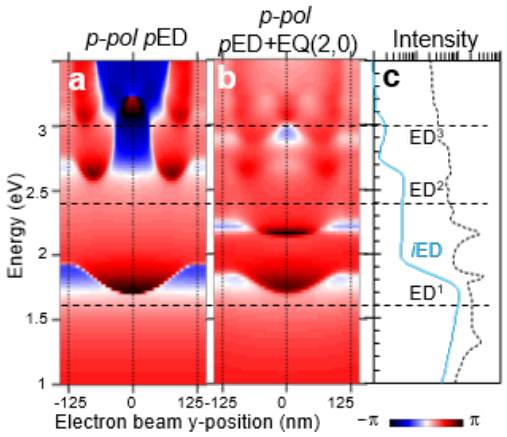

Figure S9. Spectral line profile of the emission phase calculated by using the AMD approach. (a, b) Calculated line profiles of the radiation phase of (a) the p-polarized electric field component extracted only from the pED mode with $(l, m) = (1, 0)$, and (b) the p-polarized electric field extracted only from pED and EQ (with $(l, m) = (2, 0)$ in the latter). The electron beam is scanned across the center of a 250 nm Si sphere along the y direction. The detection angle is set to $\theta = 135°$. The black vertical dotted lines at positions $y = -125$ nm, 125 nm, and 0 nm indicate the edges and the center of the sphere. (c) Integrated spectra of all the modes (dashed curve) and extracted iEDs (light blue curve) plotted in semilog scale. The energies of ED modes are indicated by horizontal dashed lines across all panels.

to the 4th order (*i.e.*, $l \leq 4$). The p-polarized total radiation plotted in Figure 4c in the main text shows an almost homogeneous phase distribution. To clarify which modes mainly contribute to this phase distribution, we calculated the spectral line profile of p-polarized pED $\{(l,m) = (1,0)\}$ and pED + EQ $\{(l,m) = (2,0)\}$ contributions, as shown in Figures S9a and b, respectively. In Figure S9a, in the photon energy range between ED^1 and ED^2, the phase is almost constant regardless of the excitation position, except in the 1.7-2.0 eV range, where the phase at the edge is reversed. Around the photon energies of ED^3, the phase is inverted well inside the sphere. This inhomogeneity of the phase is somehow canceled by including the contribution of EQ $\{(l,m) = (2,0)\}$, as shown in Figure S9b, where we plot the spectral line profile of pED + EQ $\{(l,m) = (2,0)\}$. The interference of these two modes makes the phase distribution homogeneous; they dominantly contribute to the total p-polarized radiation in such a way that the resulting phase can be used as a nearly constant reference, as shown in Figure 4c in the main text.

7. EQUIVALENCE OF BEAM ROTATION AND DETECTION ROTATION

In this section, we explain how the S_3 polar plot in Figure 8e is reconstructed. Figure 8e shows the angular radiation distribution pattern in θ and ϕ when the electron beam excites the particle at the $\phi = 0°$ edge: (x, y) =(78 nm, 0 nm). This plot is reconstructed from the θ-resolved angle dispersion patterns with $\phi = 0°$, sampled from the photon maps along the edge of the sphere. Note that this equivalence of rotating the beam with a fixed ϕ and rotating the detection angle ϕ with a fixed beam position is possible thanks to the rotational symmetry of the sample about the z axis. For instance, detection at $\phi = 0°$ with the electron beam passing near the sphere edge at (r, ϕ) =(78 nm, 90°) is identical to detection at $\phi = -90°$ with the electron beam placed at (r, ϕ) =(78 nm, 0°). This equivalence is depicted in Figure S10. Since the angular dependence on the θ angle is simultaneously obtained in each 4D STEM-CL measurement, by collecting data for different angles ϕ we can construct a polar plot in $\theta - \phi$, as shown in Figure 8e in the main text.

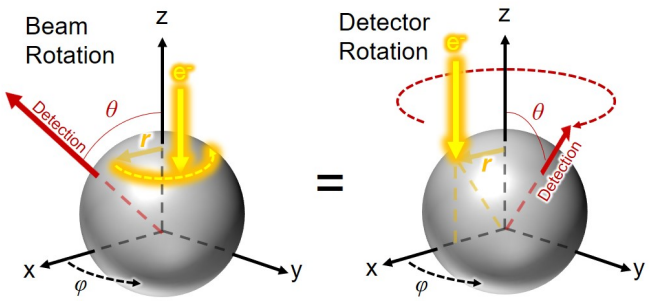

Figure S10. Schematics showing the equivalence of (left) beam rotation around the z-axis with a fixed detection angle and (right) detector rotation with a fixed electron beam position. This equivalence applies to rotationally symmetric systems, such as the individual spheres under consideration.

8. ANGULAR PLOTS REVEALING INTERFERENCE OF ED AND MD MODES

This section describes S_3 angular dispersion patterns of MD + ED interference. In Figure 8e we show the $\theta - \phi$ polar plot of S_3 at a photon energy of 2.18 eV, which is reconstructed from the photon maps at varying θ for fixed $\phi = 0°$ detection. However, the polar plot in Figure 8e gives no energy spectral informational. To complement it, we here show in Figure S11 the angular spectral patterns of S_3 and the unpolarized radiation intensity at the locations corresponding to the four S_3 *hotspots* in Figure 8d.

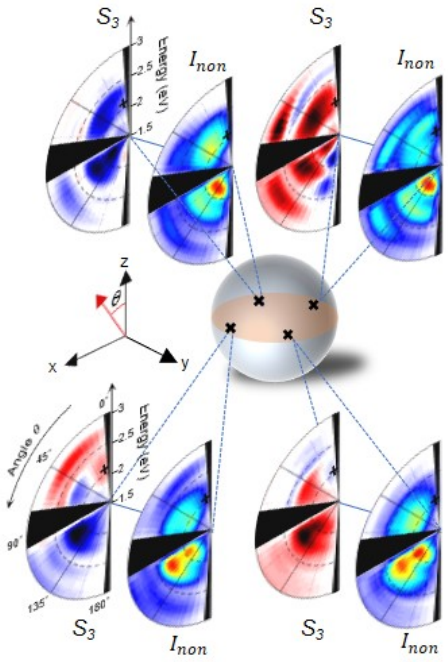

Figure S11. Angle-dispersion patterns at $\phi = 0°$ showing the Stokes parameter S_3 and the unpolarized radiation intensity at the positions corresponding to the black cross marks, namely (x, y) =(-60 nm, -60 nm), (-60 nm, 60 nm), (60 nm, -60 nm), and (60 nm, 60 nm).

---

1. García de Abajo, F. J. Relativistic Energy Loss and Induced Photon Emission in the Interaction of a Dielectric Sphere with an External Electron Beam. *Phys. Rev. B* **1999**, *59*, 3095–3107.
2. García de Abajo, F. J. Smith-Purcell Radiation Emission in Aligned Nanoparticles. *Phys. Rev. E* **2000**, *61*, 5743–5752.
3. Winther, A.; Alder, K. Relativistic Coulomb Excitation. *Nucl. Phys. A* **1979**, *319*, 518–532.
4. Abramowitz, M.; Stegun, I. A. *Handbook of Mathematical Functions*; Dover: New York, 1972; pp 771–792.
5. Low, F. E. *Classical Field Theory: Electromagnetism and Gravitation*; John Wiley & Sons: New York, 1997; pp 134–244.
6. García de Abajo, F. J. Multiple Scattering of Radiation in Clusters of Dielectrics. *Phys. Rev. B* **1999**, *60*, 6086–6102.